Effects of Cavity on the Performance of Dual Throat Nozzle During the Thrust-Vectoring Starting Transient Process

Rui Gu
e-mail: sz24zxdzb3@126.com

Jinglei Xu
Professor at NUAA
e-mail: xujl@nuaa.edu.cn

Department of Power Engineering,
Nanjing University of Aeronautics and
Astronautics (NUAA),
Nanjing 210016, China

The dual throat nozzle (DTN) technique is capable to achieve higher thrust-vectoring efficiencies than other fluidic techniques, without compromising thrust efficiency significantly during vectoring operation. The excellent performance of the DTN is mainly due to the concaved cavity. In this paper, two DTNs of different scales have been investigated by unsteady numerical simulations to compare the parameter variations and study the effects of cavity during the vector starting process. The results remind us that during the vector starting process, dynamic loads may be generated, which is a potentially challenging problem for the aircraft trim and control. [DOI: 10.1115/1.4025243]

Keywords: CFD, dual throat nozzle, thrust vectoring, internal flow, jet, unsteady flows

1 Introduction

The potential benefits of fluidic thrust vectoring nozzles over fully-mechanical techniques have been widely recognized, and have been studied in the NASA and USAF Fluidic Injection Nozzle Technology (FLINT) program [1] as: "a 28–40% weight reduction by implementing fluidic throat area control; a 43–80% weight reduction by implementing fluidic throat area and exit area control; a 7–12% improvement in engine thrust-to-weight ratio; and a 37–53% reduction in nozzle procurement and life cycle costs." In addition, fixed aperture nozzles would enhance low-detectable integration aspects by eliminating moving flaps, discontinuities, and gaps [2]. For decades the fluidic thrust vectoring nozzles have evolved four main types, shock vectoring control (SVC) [3], counter flow [4], throat shift (TS) [5,6], and dual throat nozzle (DTN) [7]. Each method uses the secondary air source in a certain way. The main results are presented briefly as follows:

Fluidic thrust vectoring with the shock vectoring control method requires asymmetric fluidic injection of a secondary air stream into the supersonic primary flow. The primary exhaust flow is then diverted through the oblique shock, which can produce large thrust-vectoring angles, but at the expense of thrust efficiency due to the oblique shock. The thrust-vectoring angle reaches a maximum at low nozzle pressure ratio (NPR) and decreases with increasing NPR [8]. The best thrust-vectoring efficiency achieved is 4.4 deg/percent injection at NPR = 3, with the thrust coefficient to be only 0.891. The thrust coefficient can be improved to 0.935 at NPR = 6, however, thrust-vectoring efficiency is reduced to 2.2 deg/percent injection. Even at the highest NPR being tested, thrust performance loss resulting from overexpansion are large [8].

In the counter flow concept, thrust vectoring is achieved by applying a vacuum to a slot adjacent to a primary jet which is shrouded by a suction collar [9]. The potential drawback is the attachment of the primary jet to the suction collar that occurs at certain conditions and various geometric configurations. The problems are hysteretic in nature and not easy to control. At NPR = 8 with jet unattached, thrust-vectoring angle is 12 deg and the thrust coefficient is 0.945. A maximum thrust-vectoring angle achieved is 15 deg at NPR = 5, but the thrust coefficient is only 0.92 [10]. Increasing ejector pressure, slot height and collar length resulted in larger thrust-vectoring angles. However, it also increased the risk of jet attachment.

In the throat shifting method, thrust vectoring is obtained by shifting the throat of the nozzle with asymmetric secondary fluidic injection. In the thrust-vectoring mode, the secondary air stream shifts the throat from the geometric minimum area to the new aerodynamic minimum area. Flow deflection then occurs in the subsonic flow region ahead of the new throat, which causes a thrust-vectoring angle with respect to the primary exhaust flow. This concept has been tested at static freestream conditions, with nozzle operating condition in the range of NPR = 1.4–4.0, and fluidic injection flow rate up to 15% of the primary flow [11]. The results show that, at NPR = 2, the throat shifted 45 deg with as little as 2% injection, but the thrust-vectoring angle is only 3.3 deg. Increasing injection flow rate to 15% increases thrust-vectoring angle to 22 deg at NPR = 2. So the thrust vectoring efficiency is only about 1.65 deg/percent injection [11].

Dual throat nozzle has been developed by NASA Langley Research Center based on the throat shifting method in 2003 [7]. The concaved cavity section is located between upstream and downstream minimum areas, and fluidic injection is introduced at the upstream minimum area location. The thrust vectoring efficiency of DTN is greater than any other fluidic thrust vectoring concept reported in the literature [12]. For example, at NPR = 4, experimental thrust vectoring efficiency is 6.1 degs/percent injection and thrust coefficient is 0.968, which only results in 0.5% more loss compared to nonvectoring case. Dual throat nozzle technique does not compromise system thrust coefficient, unlike shock vectoring control method which will incur large thrust penalties with the creation of the shock required for deflecting the flow [13]. Different configurations of DTN have been studied. In addition to the two-dimensional configuration, an axisymmetric DTN for a supersonic aircraft application has also been computationally and experimentally studied [14,15]. The aerodynamic performance is analyzed and the geometry is optimized [16]. There remains a lot of research work to get a greater thrust vectoring angle under different NPRs, but very little has been done to study the effects of cavity size on the performance of DTN, although the excellent performance of the DTN is mainly due to the cavity. Especially, with respect to the open cavity flow [17], the dynamic interactions between traveling vortices in the shear layer are complex [18,19]. An obvious recirculation zone often appears in the cavity section, showing that there may exist some aerodynamic hysteresis on the DTN performance. How does the recirculation zone change during the vector starting process? How does scaling affect the dynamic response time and the thrust vectoring angle, especially with different scales of the cavity? The studies were mainly based on the down-scaled model experiments, how about the performances of the real size?

To answer these questions, two DTN models were studied with different scales using unsteady simulations. The complex flow field, unsteady phenomena and the mechanisms are analyzed carefully in this article. Especially the negative thrust vectoring angle appearing at the beginning of the vector starting process is found, and the mechanisms are discussed.

In Sec. 2, the numerical simulation model is discussed. Section 3 presents the results of the simulations and finally, conclusions are given in Sec. 4.

Contributed by the Turbomachinery Committee of ASME for publication in the Journal of Engineering for Gas Turbines and Power. Manuscript received July 3, 2013; final manuscript received July 31, 2013; published online October 21, 2013. Editor: David Wisler.

2 Numerical Simulation Model

2.1 Computation Domain and DTN Operating Conditions. The model simulated in this paper is a two-dimensional (2D) dual throat nozzle, as shown in Fig. 1. The scale nuzzled is labeled Case 1 and the real size nozzle is labeled Case 2. The Case 1 geometry is defined as follows: Divergence angle of the concaved cavity (A) is 13.5 deg; convergence angle of the concaved cavity (B) is 39 deg, injection angle of the secondary flow (C) is 15 deg; upstream throat height (Throat) is 20 mm, SEC = 0.1 × Throat, L = 3.5 × Throat, Outlet = Throat. For the real size nozzle, the throat of Case 2 is chosen as 200 mm, while the other geometric parameters including conversion relations are all with the same as Case 1. Thus, the scale of Case 2 is ten times of Case 1. The operating conditions are chosen as follows: Total temperatures of the primary and secondary flows are 300 K; NPR is 3; Total pressure of the mainstream is 1.5 times of that of the secondary flow. The simulation was conducted in two phases: First, secondary flow was turned off and the steady state flow field with no vectoring was calculated. Then, secondary flow was turned on and time-dependent flow field was calculated starting from the steady state solution. The time step was 0.01 ms during the unsteady flow field calculation.

2.2 Governing Equations. The jet in the present study is considered to be unsteady, two-dimensional, turbulent, and compressible flow. The density is defined by the ideal gas law. The dynamic viscosity is assumed to be constant, and the gravity effect can be neglected. Based on these assumptions, the conservation equations, together with the ideal gas law, can be expressed as follows:

Momentum

$$\rho\left(u_j\frac{\partial u_i}{\partial x_j}\right) = -\frac{\partial p}{\partial x_i} + \frac{\partial}{\partial x_j}\left(\mu\frac{\partial u_i}{\partial x_j} - \overline{\rho u_i' u_j'}\right) \tag{1}$$

Continuity

$$\frac{\partial(\rho u_i)}{\partial x_i} = 0 \tag{2}$$

Ideal Gas Law

$$P = \rho RT \tag{3}$$

2.3 Turbulence Model. In this study, 2-D unsteady viscous Navier–Stokes equations are solved, with RNG k-ε turbulence model and standard wall function in the flow field. To verify the capacity of such a simulation method, the solver was firstly validated against experimental data [14].

The numerical simulation and experiment data comparison is illustrated in Fig. 2. Comparison between experimental and computational results of upper-wall pressure is shown in Fig. 3. It is found that the numerical method could clearly resolve the detailed flow field and the calculated upper-wall static pressure agrees with the experiment data very well. Therefore, the RNG k-turbulence model with the standard wall function is employed for the current study.

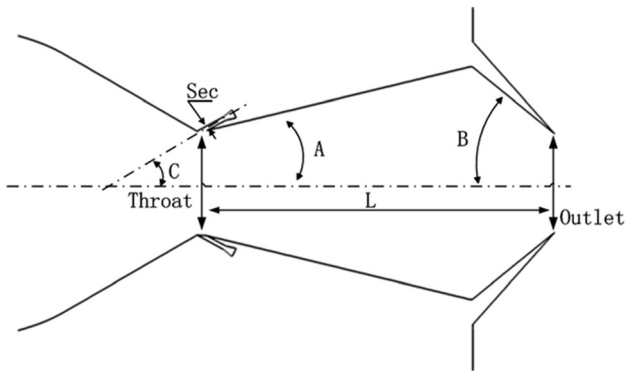

Fig. 1 Sketch of the dual throat fluidic thrust vectoring nozzle

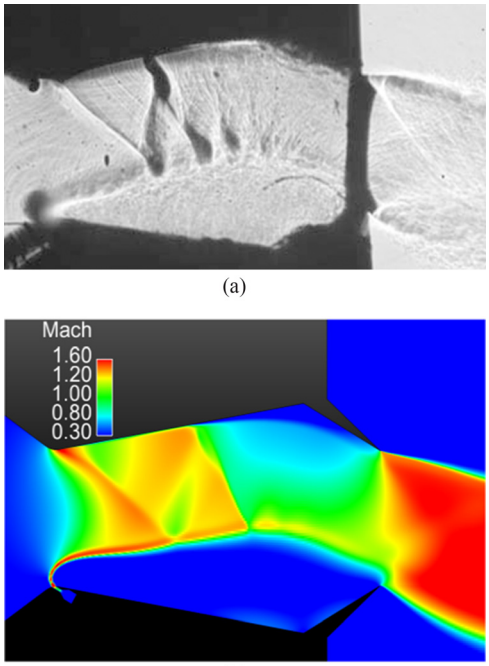

(a)

(b)

Fig. 2 Numerical simulation and experiment results comparison. (*a*) Experimental shadowgraph image [10]; (*b*) Mach contour of simulation.

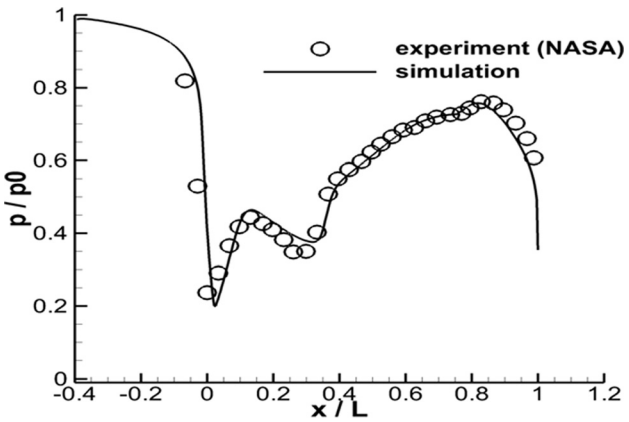

Fig. 3 Comparison of experimental and computational upper-wall pressure

2.4 Computational Mesh. Structured meshes are generated for the DTN's computation domain using ICEM, as shown in Fig. 4. The grids near the nozzle wall have been refined using the boundary-layer setting function. The displacement of the first layer thickness of the wall is set as 0.02 mm. The meshes are clustered near the cavity region. In the streamwise (or x) direction, the initial spacing of the nodes is set at 0.3 mm. A mesh independence study was conducted with the following node distributions of the core region: 80×120 (coarse), 120×180 (medium), and 150×220 (fine). The pressure distribution on the upper wall along the flow direction obtained for different grids are shown in Fig. 5. It can be found that the differences between the medium grid case

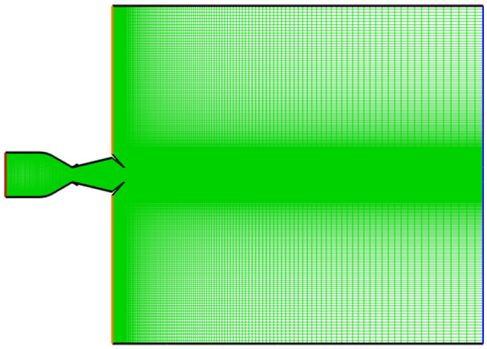

(a)

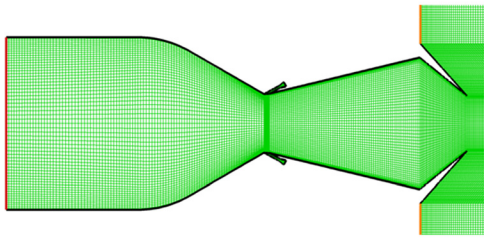

(b)

Fig. 4 Computational mesh. (*a*) Computational mesh for the domain; (*b*) zoomed in computational mesh at the nozzle.

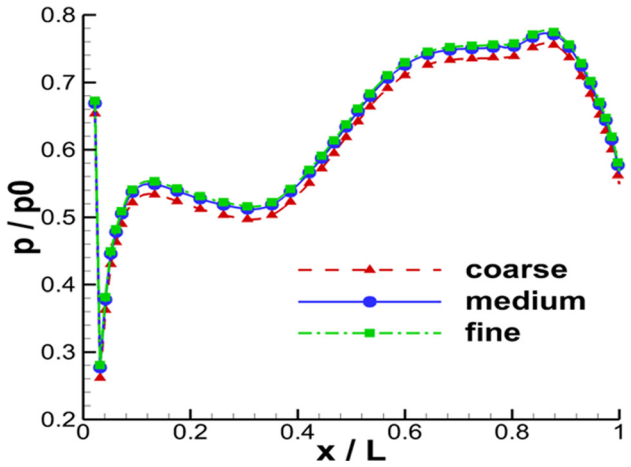

Fig. 5 Pressure distributions of different grids on the upper-wall

and the fine grid cases are all within 1%. As a result, the medium grid resolution was chosen for further investigations. The numerical computations were conducted by the finite volume method developed by Patankar [20] via the commercial computational fluid dynamics (CFD) code (ANSYS FLUENT 13.0). The conservation equations for momentum and density-based continuity are solved together by the coupled algorithm.

3 Results and Analysis

The nozzle performances of Case 1 during the vector starting process are shown in Fig. 6. The variation of thrust vectoring angle is given in Fig. 6(*a*). It is found that the vectoring angle decreases from zero to a negative value at the beginning of the vectoring process, and then drops rapidly to the minimum. After that, the vectoring angle recovers from negative to the zero, and goes up quickly, until it approaches its maximum. Then it oscillates for about 2.5 ms and finally approaches to a stable, positive vectoring angle. Before approaching the effective vectoring angle,

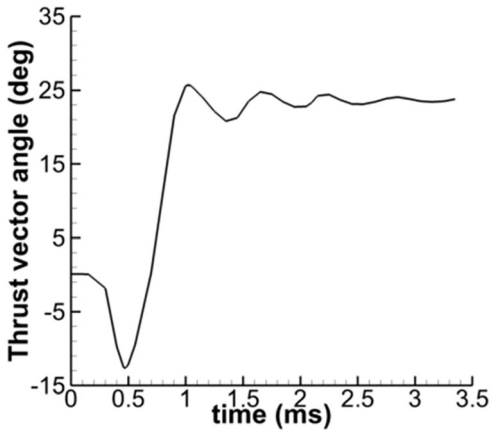

(a)

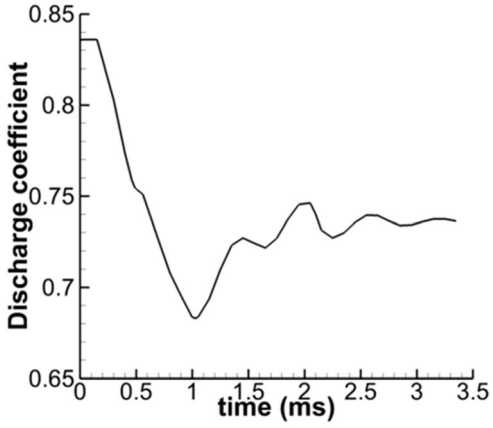

(b)

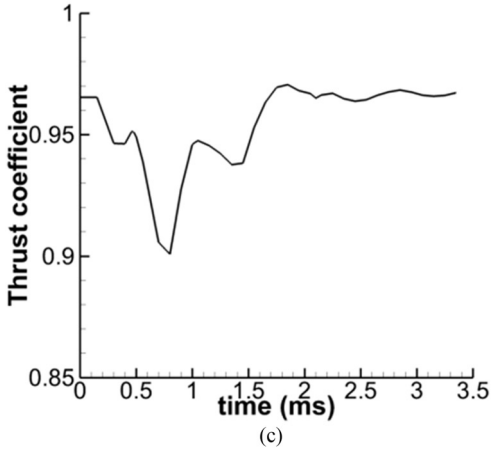

(c)

Fig. 6 Nozzle performance of Case 1 during the vector starting process. (*a*) Thrust vector angle; (*b*) discharge coefficient; and (*c*) thrust coefficient.

the maximum magnitude of the negative vectoring angle is about the 60% of the maximum positive one. It takes about 0.5 ms to recover from the maximum negative vectoring angle to the maximum positive one. Therefore, the vectoring angle changing rate is nearly 78 deg per millisecond, and the vector starting process is complex and unsteady. So as far as we know, there is no relative report about this phenomenon yet. The variation of the discharge coefficient during the process is shown in Fig. 6(*b*). Because of the secondary flow, the real throat area and the discharge coefficient are all decreased. The variation of the thrust coefficient during the process is shown in Fig. 6(*c*), which shows the fluctuation amplitude due to the abrupt changes of the flow field is about 6.5% of the mean value.

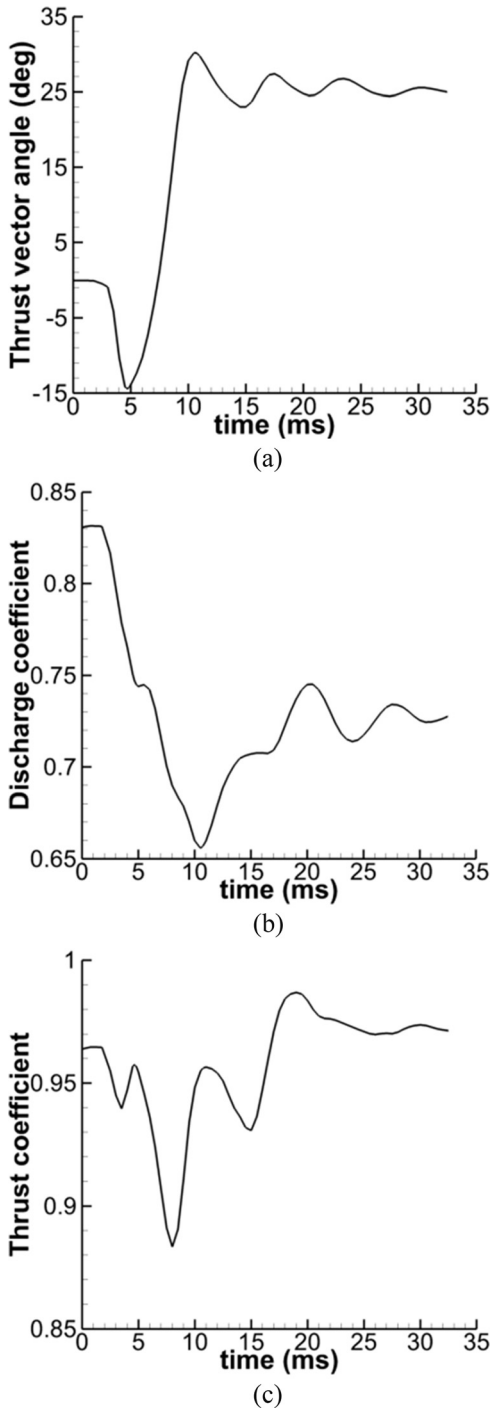

Fig. 7 Nozzle performance of Case 2 during the vector starting process. (*a*) Thrust vector angle; (*b*) discharge coefficient; and (*c*) thrust coefficient.

The variations of the aerodynamic performances of the Case 2 with time during the vector starting process are shown in Figs. 7(*a*), 7(*b*), and 7(*c*), which show the variations of thrust vectoring angle, discharge coefficient and thrust coefficient, respectively. It can be found that, the variation trends of the corresponding parameters in the two cases are very similar. But the dynamic response time of Case 2 is about ten times as that of the Case 1 by comparing the time of the peak value. After the vectoring angle approaches stable, the performance is almost the same. For example, the thrust vectoring angle of Case 1 is 23.78 deg and 24.99 deg for Case 2; the discharge coefficients are 0.736 and 0.728, respectively; and the thrust coefficients of the two cases are 0.967 and 0.971, respectively. Therefore, if the model is enlarged ten times, the discharge coefficient reduces slightly, the thrust coefficient increases a bit, and the vectoring angle increases about 5%.

The dynamic process of the vector starting is also clearly shown as follows. At the initial moment, a vortex-pair is generated in the cavity. In this paper, the upper one is defined as Vortex A, and the lower one is defined as Vortex B. They rotate oppositely with the same intensity, so no vectoring angle is generated. The vorticity contour, pressure contour and the velocity vector of Case 2 at different times are shown in Fig. 8 and Fig. 9, respectively. Because

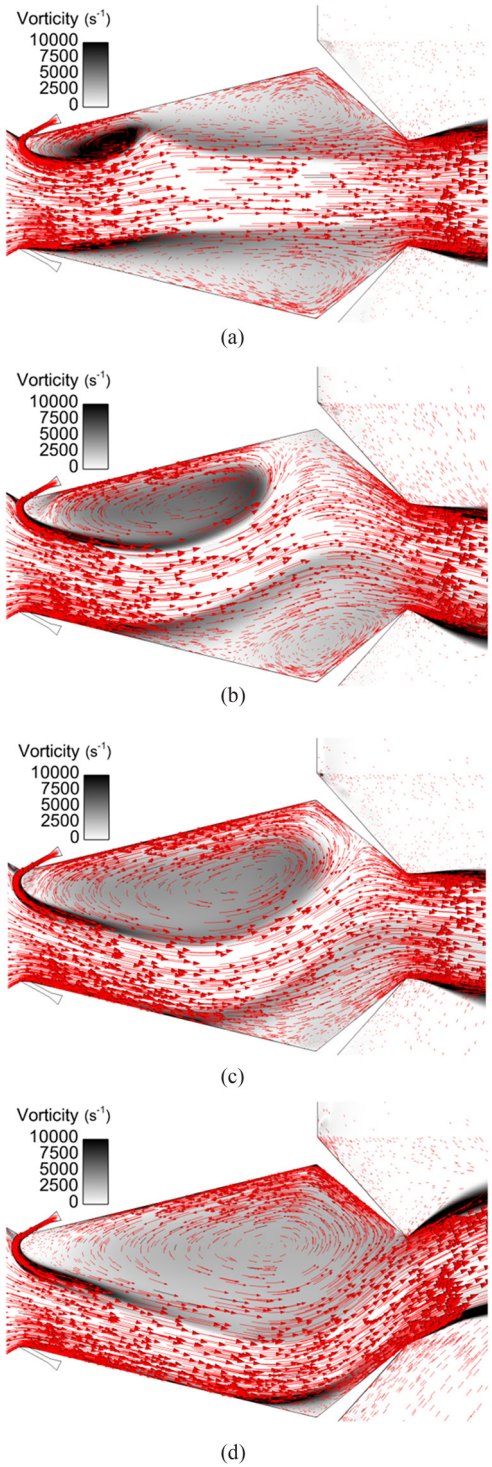

Fig. 8 Vorticity contour and velocity vector of Case 2. (*a*) 1.5 ms; (*b*) 5 ms; (*c*) 7 ms; and 8 (*d*) 10 ms.

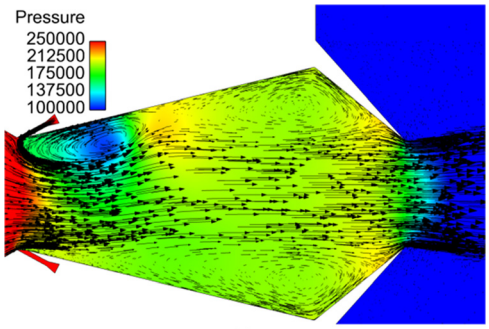

(a)

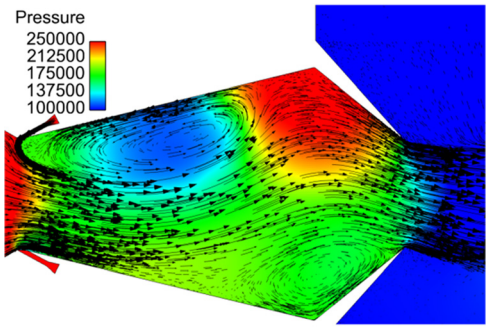

(b)

Fig. 9 Pressure contour and velocity vector of Case 2. (*a*) 1.5 ms; and (*b*). 5 ms.

of the issuing of the secondary flow, the effective aerodynamic throat is formed near the first minimum area and the throat is skewed downstream. Then due to the viscous shearing effect between the secondary flow and mainstream, a new vortex, labeled as Vortex C, is formed on the upper side. Because the rotation directions between Vortex A and Vortex C are the same, they repel each other. So high pressure zone appears near the interface, as showed in Fig. 8(*a*). The vorticity of Vortex C is greater than that of the Vortex A, so the size of Vortex A is decreased. The open cavity flow on the upper side wall is changed to closed cavity flow. Then at 5 ms, Vortex C develops rapidly and occupies about 25% of the cavity volume, and the Vortex A has been completely disappeared. Induced by Vortex C, the mainstream impinges on the upper convergence zone, and the high pressure zone appears, as shown in Fig. 8(*b*). Vortex B is induced by the Vortex C and expands to the upper side. And the left side area of the Vortex B is reduced due to the combination effect of the mainstream and the Vortex C. The mainstream appears as S shape, with the thrust vectoring angle as – 14 deg at this moment. At 7 ms, Vortex C occupies about 40% of the cavity and the size of Vortex B is reduced by 60%. The mainstream is induced by Vortex C and is divided into two parts. One part still impinges on the upper convergence zone, and the other issues directly to the nozzle exit, as shown in Fig. 8(*c*). At 10 ms, Vortex C occupies about 60% cavity area and Vortex B is nearly disappeared except for minimum backflow zone in the bottom of the cavity. Vortex C induces the mainstream flow to the nozzle exit, and the closed cavity flow on the upper side is recovered to the open cavity flow again. Now the thrust vectoring angle approaches its maximum value of about 29 deg, as shown in Fig. 8(*d*). The relationship between the Vortex C and the vectoring angle is very close. Generally speaking, the greater the vorticity, the more obvious of the inducing effect, and the greater vectoring angle that the nozzle could achieve.

The sketch of vortex interaction during the vector starting process is shown in Fig. 10. There are three major vortices in the DTN, namely the Vortex A, Vortex B and Vortex C. As discussed above, Vortex A and Vortex B are induced by mainstream at the

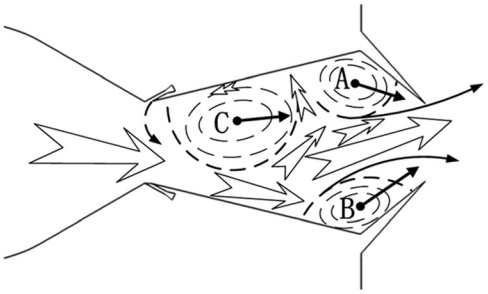

Fig. 10 Sketch of vortex interaction in the DTN

initial moment. The flow structures are open cavity flow. Vortex C is mainly induced by the secondary flow. There is mutual repulsion between Vortex A and Vortex C. The flow structure of upper side changes to closed cavity flow. Due to the effect of Vortex C, the sizes of Vortex A and Vortex B are reduced. After Vortex A disappears, the mainstream impinges on the upper convergence zone induced by Vortex C, which causes the pressure increasing in the zone. This mechanism makes the thrust vectoring angle negative at the beginning of the starting process. After Vortex B almost disappears, Vortex C occupies the cavity alone, and the mainstream forms a stable positively vectoring jet. The flow structure of the upper side goes back to open cavity flow.

4 Conclusions

Two different scales of the dual throat fluidic thrust vectoring nozzle are studied by time-dependent numerical simulation. The effects of cavity are analyzed during the vector starting process. The following conclusions could be drawn: (1) Before the nozzle produces the effective positive vectoring angle, a negative vectoring angle appears at first, which has a magnitude of about the 60% of the maximum positive vectoring angle. And it takes about 0.5 ms to recover from the maximum negative vectoring angle to the maximum positive one; (2) During the vector starting process, the vectoring angle changing rate is quite large. In Case1 of this study, the vectoring angle changing rate is nearly 78 deg per millisecond. (3) As the scale of the DTN nozzle is enlarged tenfold, the dynamic responding time is also increased almost by a factor of 10. Under the same operating conditions, the larger model can get a higher thrust vectoring angle by about 5%. (4) The vector starting process is complex and unsteady. The two original vortices are dissipated and a new vortex induced by secondary flow occupies the cavity eventually and the dynamic response time is very short. Therefore, during the vector starting process, a negative vector cannot be ignored. The dynamic response of vectoring angle will lead to dynamic load, and the nozzle may lose stability, which is a real challenge to the control system.

Acknowledgment

We would like to acknowledge the continued support of China Gas Turbine Research Institute Research Program.

Nomenclature

A = divergence angle of the concaved cavity
B = convergence angle of the concaved cavity
C = injection angle of the secondary flow
DTN = dual throat nozzle
L = cavity length
NPR = nozzle pressure ratio
Outlet = nozzle outlet height
Sec = secondary flow injection height
SVC = shock vectoring control
Throat = upstream throat height
TS = throat shifting

References

[1] Walker, S. H., 1997, "Lessons Learned in the Development of a National Cooperative Program," AIAA Paper No. 97-3348.
[2] Deere, K. A., 1997, "Summary of Fluidic Thrust Vectoring Research Conducted at NASA Langley Research Center," AIAA Paper No. 2003-3800.
[3] Deere, K. A., 2000, "Computational Investigation of the Aerodynamic Effects on Fluidic Thrust Vectoring," AIAA Paper No. 2000-3598.
[4] YonhHeo, J., and Sung, H.-G., 2012, "Fluid Thrust-Vector Control of Supersonic Jet Using Coflow Injection," J. Propul. Power, **28**(4), pp. 858–861.
[5] Miller, D. N., Yagle, P. J., and Hamstra, J. W., 1999, "Fluidic Throat Skewing for Thrust Vectoring in Fixed-Geometry Nozzles," AIAA Paper No. 99-0365.
[6] Williams, R. G., and Vittal, B. R., 2002, "Fluidic Thrust Vectoring and Throat Control Exhaust Nozzle," AIAA Paper No. 2002-4060.
[7] Shin, C., and Dong Kim, H., 2010, "A Computational Study of Thrust Vectoring Control Using Dual Throat Nozzle," J. Therm. Sci., **19**(6), pp. 486–490.
[8] Abeyounis, W. K., and Bennett, B. D., Jr., 1997, "Static Internal Performance of an Over Expanded Fixed-Geometry, Nonaxisymmetric Nozzle With Fluidic Pitch-Thrust-Vectoring Capability," NASA Paper No. TP-3645.
[9] Strykowski, P. J., and Krothapalli, A., 1993, "The Countercurrent Mixing Layer: Strategies for Shear-Layer Control," AIAA Paper No. 93-3260.
[10] Flamm, J. D., 1998, "Experimental Study of a Nozzle Using Fluidic Counterflow for Thrust Vectoring," AIAA Paper No. 98-3255.
[11] Deere, K.A, 1998, "PAB3D Simulation of a Nozzle With Fluidic Injection For Yaw Thrust-Vector Control," AIAA Paper No. 98-3254.
[12] Deere, K. A., Berrier, B. L., Flamm, J. D., and Johnson, S. K., 2005, "A Computational Study of a Dual Throat Fluidic Thrust Vectoring Nozzle Concept," AIAA Paper No. 2005-3502.
[13] Flamm, J. D., Deere, K. A., Berrier, B. L., and Johnson, S. K., 2005, "An Experimental Study of a Dual Throat Fluidic Thrust Vectoring Nozzle Concept," AIAA Paper No. 2005-3503.
[14] Deere, K. A., Flamm, J. D., Berrier, B. L., and Johnson, S. K., 2007, "Computational Study of an Axisymmetric Dual Throat Fluidic Thrust Vectoring Nozzle for a Supersonic Aircraft Application," AIAA Paper No. 2007-5085.
[15] Deere, K. A., Flamm, J. D., Berrier, B. L., and Johnson, S. K. 2007, "Experimental Study of an Axisymmetric Dual Throat Fluidic Thrust Vectoring Nozzle Concept for Supersonic Aircraft Application," AIAA Paper No. 2007-5084.
[16] Flamm, J. D., Deere, K. A., Mason, M. L., Berrier, B. L., and Johnson, S. K., 2006, "Design Enhancements of the Two-Dimensional, Dual Throat Fluidic Thrust Vectoring Nozzle Concept," AIAA Paper No. 2006-3701.
[17] Radhakrishnan, S., and Meganathan, A. J., 2002, "Open Cavity Flow at Subsonic Speeds—Comparison of Numerical Simulations With Experiments," AIAA Paper No. 2002-0571.
[18] Li, Z., Li, J., and Yan, X., 2011, "Effects of Pressure Ratio and Rotational Speed on Leakage Flow and Cavity Pressure in the Staggered Labyrinth Seal," ASME J. Eng. Gas Turbines Power, **133**(11), p. 114503.
[19] Ganine, V., Umesh, J., and Hills, N., 2012, "Coupled Fluid-Structure Transient Thermal Analysis of a Gas Turbine Internal Air System With Multiple Cavities," ASME J. Eng. Gas Turbines Power, **134**(10), pp. 102508.
[20] Patankar, S. V., 1980, *Numerical Heat Transfer and Fluid Flow*, McGraw-Hill, New York, pp. 89–109.